Non-plume flood basalt volcanism before the emplacement of the Afar mantle plume head

Yutaka Yoshimura[1,2], Osamu Ishizuka[3,4], Toshitsugu Yamazaki[2], Hyeon-Seon Ahn[5], Tesfaye Kidane[6], Yuhji Yamamoto[7], Shun Sekimoto[8], Yo-ichiro Otofuji[9,10]

[1] Department of Environmental Changes, Faculty of Social and Cultural Studies, Kyushu University
[2] Atmosphere and Ocean Research Institute, the University of Tokyo
[3] Institute of Earthquake and Volcano Geology, Geological Survey of Japan, AIST
[4] Japan Agency for Marine-Earth Science and Technology
[5] Quaternary Environment Research Center, Climate Change Response Division, Korea Institute of Geoscience and Mineral Resources (KIGAM)
[6] School of Agricultural, Earth, and Environmental Sciences, University of KwaZulu Natal
[7] Center for Advanced Marine Core Research, Kochi University
[8] Institute for Integrated Radiation and Nuclear Science, Kyoto University
[9] Institute of GeoHistory, Japan Geochronology Network
[10] Kobe University

Corresponding author: Yutaka Yoshimura (yoshimura.yutaka.36w@kyoto-u.jp)

Key Points:

- We obtain two new $^{40}Ar/^{39}Ar$ ages for the low-Ti basalt from the Lima-Limo section of the Ethiopia–Yemen flood basalts
- Based on our eruptive age model, we correlate the Lima-Limo section to Chrons C12r to C11r
- We conclude that the non-plume low-Ti basalts erupted before the Afar plume high-Ti basalts because of the plume–lithosphere interaction

Abstract

The Ethiopia-Yemen flood basalts are spatially zoned with progressively lower TiO_2 lavas from near the Afar depression toward the margins. The timing and rate of emplacement of low TiO_2 (LT) lavas are poorly known compared with the ultra-high TiO_2 (HT2) lavas. We measured two high-precision $^{40}Ar/^{39}Ar$ ages of 29.63 ± 0.14 and 30.02 ± 0.22 Ma (2σ) from basalts of the 2-km-thick LT lava sequence at the Afar plume head margin. Using our eruption age model constructed from our and previous $^{40}Ar/^{39}Ar$ ages with the paleomagnetic directions, we estimate that the LT lava eruption continued over Chrons C12r-C12n-C11r. The eruption of the plume head margin started earlier than the plume head axis emplacement in C12n. Also, the eruption rate was low at the margin, high at the axis. We estimate that the LT lavas are induced by the edge-driven convection, the result of a plume-lithosphere interaction, not a plume head.

Plain Language Summary

The Ethiopia-Yemen Flood Basalts are the expression of a mantle plume erupting millions of km^3 of basaltic lava in a geologically short period (1-3 million years (Myr)). Titanium concentrations in the flood basalts are zoned and named HT2, HT1, and LT basalts (from high to low Ti). The eruption timing and rate of the HT2 basalts are constrained with high precision, but those of the LT basalts remain ambiguous. Therefore, we measured two high-precision $^{40}Ar/^{39}Ar$ ages from LT basalts in the 2-km-thick Lima-Limo section, which erupted northwest of the Afar area. Based on our eruption age model constructed from $^{40}Ar/^{39}Ar$ ages and paleomagnetic directions, we estimate that the eruption of the LT basalts started earlier than the HT2 basalts that erupted in Chron C12n and lasted over at most ~2 Myr. The eruptive rate of the LT basalts (0.02-4.69 km^3/yr) in the earliest interval was lower than that of the HT2 basalts (4-13 km^3/yr). We may explain that this eruption feature by a thickness gradient in the lithosphere on the Afar mantle plume at that time.

1 Introduction

Understanding of the flood basalt eruptions is essential because it provides clues to past mantle plume activity. The Afar Plume formed the Afro–Arabian Large Igneous Province (AALIP) over three periods, the Eocene, Oligocene, and Miocene (Rooney, 2017), and is one of the freshest flood basalts on Earth. The most active emplacement of AALIP occurred in the Oligocene (e.g., Hofmann et al., 1997), called the Oligocene Ethiopian–Yemen Traps, and geochemical studies of the Oligocene flood basalts have clarified that basalts show zoning with Ti content (Pik et al., 1998). Low Ti tholeiitic lavas (LT, TiO_2: 1–3 wt%) occur in the western part, high Ti tholeiitic lavas (HT1, TiO_2: 2–4 wt%) in the eastern part, and ultra-high Ti transitional basalt/picrite lavas (HT2, TiO_2 3–7 wt %) near the Afar triple junction (Fig. 1a) (Pik et al., 1998; Beccaluva et al., 2009; Natali et al., 2016; Rooney, 2017). HT2 lava has a high mantle potential temperature (Beccaluva et al., 2009; Natali et al., 2016). Since high $^4He/^3He$ ratios were reported from HT2 lava, it is thought to be of deep mantle origin, consistent with the plume hypothesis (Marty et al., 1996; Natali et al., 2016). Mantle seismic tomography also suggests that the Afar plume rises from the bottom of the lower mantle (French and Romanowicz, 2015; Boyce et al., 2021). The HT2 basalts are the earliest eruptions of the Oligocene Ethiopia–Yemen Traps and are estimated to have significantly high emplacement rates (Eid et al., 2021). However, the timing and rate of the emplacement of LT lavas have not been uniquely determined, and their eruption rates remain ambiguous (Fig. 1b) (Ahn et al., 2021; Eid et al., 2021).

The Oligocene Ethiopia–Yemen Traps are one of the three volcanic pulses of AALIP from the Eocene to the Miocene (Rooney, 2017). In the Lima-Limo section of the Traps, one of the thickest LT basalt sections in northwestern Ethiopia (Fig. 1a), several studies on paleomagnetism and $^{40}Ar/^{39}Ar$ age estimated that its eruption duration is 0.8–1.5 million years or less (Myr) (Hofmann et al., 1997; Rochette et al., 1998; Coulié et al., 2003; Ahn et al., 2021). Hofmann et al. (1997) and Rochette et al. (1998) conducted a magnetostratigraphic and $^{40}Ar/^{39}Ar$ study of the Lima-Limo section of the Traps and interpreted that the main part of the Traps erupted at about 30 Ma in a short period of time, less than 1.5 Myr. They identified a R–N–R polarity sequence and correlated it with Chrons C11r–C11n or C11r–C10r in the Geomagnetic Polarity Time Scale (GPTS) of Heustis and Acton (1997) (Fig. 1b). Coulié et al. (2003) performed K/Ar and $^{40}Ar/^{39}Ar$ datings and improved the correlation of the magnetostratigraphy of Rochette et al. (1998) with GPTS of Cande and Kent (1995) (Fig. 1b). However, previous studies couldn't establish a unique magnetostratigraphic correlation with GPTS (Fig. 1b). Recently, seven magnetozones were identified from the Traps: R1–N1–R2–N2–R3–N3–R4, from the bottom to the top of the section (Ahn et al., 2021). These newly found magnetozones make unique correlations to GPTS more difficult. The reason for the lack of the unique magnetostratigraphic correlation of the Lima-Limo section in previous studies is that they did not construct any eruption age models using the $^{40}Ar/^{39}Ar$ ages, which should be based on a common standard age. Furthermore, it is necessary to use as many $^{40}Ar/^{39}Ar$ ages as possible in order to construct high-precision age models. Therefore, in this paper, we report new high-precision $^{40}Ar/^{39}Ar$ ages of lavas from the Lima-Limo section and combine them with previously reported $^{40}Ar/^{39}Ar$ ages and construct an age model to estimate the eruption timing and rate.

2 Geological Setting, Samples and Methods

2.1 Geological Setting

The Oligocene Ethiopia–Yemen Traps in the Lima-Limo section erupted at ~30 Ma (Hofmann et al., 1997; Rochette et al., 1998; Coulié et al., 2003), which was before the Afro-Arabian continental breakup (Bosworth et al., 2005). Continuous lava piles that erupted at ~30 Ma have also been found in other areas of Ethiopia (e.g., Prave et al., 2016; Lhuillier and Gilder, 2019; Eid et al., 2021). After the continental breakup, the Traps split into two parts, 90% in Ethiopia and 10% in the Arabian Peninsula (Fig. 1a). Currently, the area of the main part of the Traps in Ethiopia is ~600,000 km^2 (Mohr, 1983). The total lava thickness of the Lima-Limo section reaches ~2 km, and all lava flows are LT basalts. The total volume of the Oligocene Ethiopia–Yemen Traps is estimated to be 350000 km^3 (Mohr, 1983; Mohr and Zanettin, 1988). The lower part (<~2200 m) is characterized by thin lava flows (<10 m) and a gentle slope morphology. In contrast, the upper part (>~2200 m) consists mainly of thick lava flows (10–100 m), forming cliffs with clear breaks along flow contacts (Ahn et al., 2021). In the Oligocene Ethiopia–Yemen Traps consisting of a large range of compositions from low-Ti to high-Ti basalts, in particular, the eruption rate of HT2 basalt in the Waja section may have been higher than that of LT basalt in the Belessa and Lima-Limo sections (Eid et al., 2021).

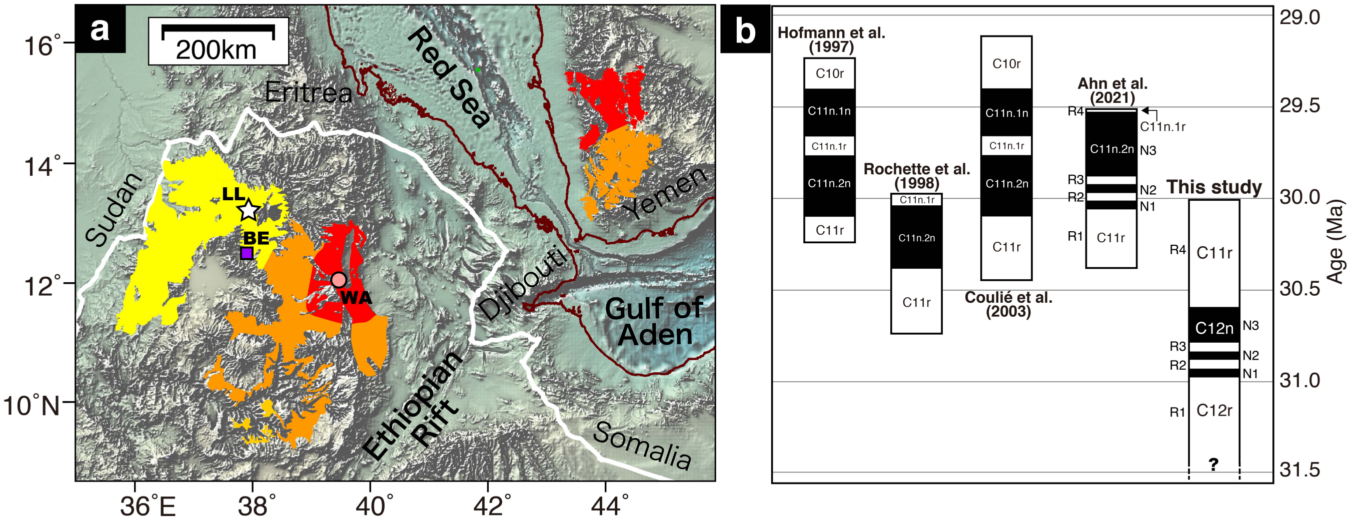

Figure 1. (a) Schematic map of the Oligocene Ethiopia–Yemen Traps (after Rooney, 2017). Section names are: Lima-Limo (LL, this study), Belessa (BE), and Waja (WA). Yellow, orange, and red colors show the spatial distribution of the basalt lavas of different titanium concentrations (Pik et al., 1998): LT, TiO_2 1–3 wt%, HT1, TiO_2 2–4 wt%, and HT2, TiO_2 3–7 wt%. The thick white line indicate the Ethiopian border. (b) Summary of previous and our magnetostratigraphic correlations of the Lima-Limo section. The reference GPTS are Cande and Kent (1995) for Hofmann et al. (1997), Huestis and Acton (1997) for Rochette et al. (1998), Cande and Kent (1995) for Coulié et al. (2003), Ogg et al. (2016) for Ahn et al. (2021), and Ogg (2020) for this study. When alternative age correlations were proposed in the previous studies, only the correlations preferred by the original authors in each study are presented here. We label the geomagnetic reversals in Chron C12n as the 'Lima-Limo reversals' and assumed that the Lima-Limo reversals are evenly distributed over the early half of Chron C12n.

2.2 Samples

We used the same LT lava samples as those in previous paleomagnetic studies (Fig. 1a, S1) (Yoshimura et al., 2020; Ahn et al., 2021). Before the dating experiments, we selected samples by inspecting thin sections to avoid contamination from secondary minerals. Photographs of the thin sections are shown in Fig. S2. Samples A1–61 and A2–162 are from two reversely magnetized lava flows belonging to the R4 magnetozone. Samples A2–482 and A2–604 are from the normally magnetized lava flows of the N3 and N1 magnetozones, respectively.

2.3 $^{40}Ar/^{39}Ar$ dating

We determined the ages of the basalt samples from the Lima-Limo section using the $^{40}Ar/^{39}Ar$ dating instrument at the Geological Survey of Japan, AIST. The details of the procedures are described in Ishizuka et al. (2018) and Text S1.

2.4 Eruption age model

We calculated Bayesian eruption age models using MacBacon 2.2 (Blaauw and Christen, 2011) and applied the following prior distributions: acc.shape = 1.5; acc.mean = 500; mem.strength = 4, mem.mean = 0.7, thick = 125 (same as Sprain et al., 2019 except for the "thick").

3 Results

Four samples were dated by stepwise heating analysis (Tables S1 and S2; Fig. 2a). Two samples (A1–61 and A2–162) yielded well-defined age plateaus comprising 82.7% and 82.1% of released gas, respectively (Tables S1 and S2; Fig. 2a). The inverse isochron ages for the two age spectra are identical to the weighted average ages of plateau-forming steps within 2σ error (Table S1, Fig. S3). These data indicate that the two plateau ages (29.63 ± 0.14 Ma for sample A1–61 and 30.02 ± 0.22 Ma for sample A2–162) (2σ, respectively) are reliable eruption ages of the basalts. A2–482 showed a partially disturbed age spectrum comprising 44.9% of released gas and did not have a plateau in a strict mean (Tables S1, S2; Fig. 2a). Sample A2–604 gave an age spectrum comprising 43.5% of the released gas and did not exhibit a plateau in a strict mean either (Tables S1 and S2; Fig. 2a). The age spectrum includes some apparent disturbance in low-temperature steps due to ^{39}Ar recoil (Schaen et al., 2020). Thus, we do not use the ages (samples A2-604 and A2-482) in our discussion.

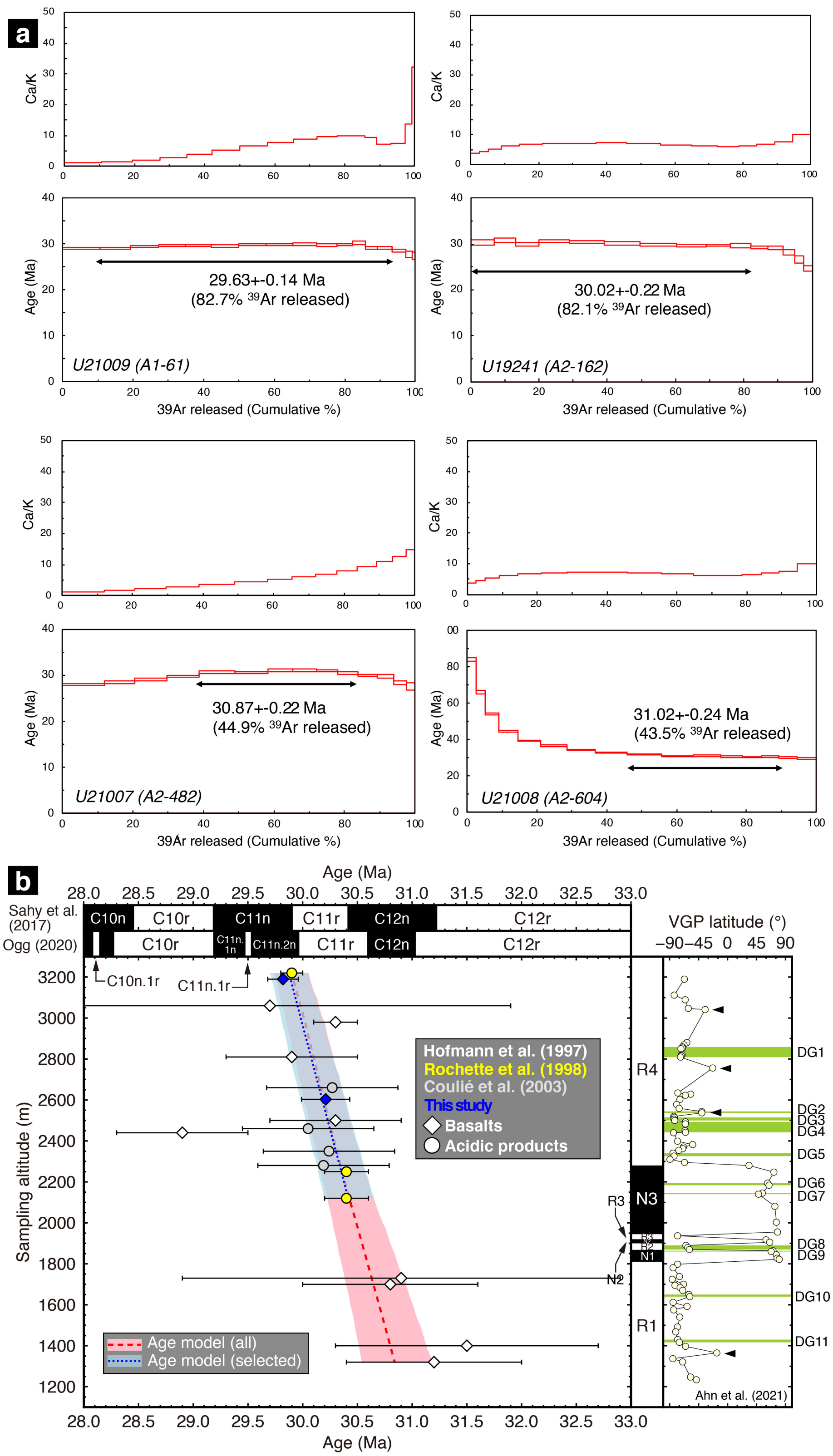

Figure 2. (a) $^{40}Ar/^{39}Ar$ age spectra and Ca/K plots for leached groundmass samples. Arrows indicate the steps forming plateau ages. $^{40}Ar/^{39}Ar$ plateau ages are shown with 2σ error. (b)

Bayesian eruption age models and compilation of our $^{40}Ar/^{39}Ar$ ages for the Lima-Limo section together with previously reported $^{40}Ar/^{39}Ar$ ages (Hofmann et al., 1997; Rochette et al., 1997; Coulié et al., 2003) with altitude (2σ error). The age model with the red dashed (blue dotted) line and the pink (light blue) area is for all ages (selected ages: this study and Rochette et al., 1998). The lines are averages of the age models, and the colored areas show 95% confidence intervals. Bayesian age model Bacon (Blaauw and Christeny, 2011) was used. All $^{40}Ar/^{39}Ar$ ages are recalibrated to the FCs standard with an age of 28.201 Ma (Kuiper et al., 2008) and the ^{40}K decay constant (Min et al., 2000). The Lima-Limo magnetostratigraphy, VGP latitudes, and paleomagnetic directional groups (DGs) (yellow green shaded boxes) (Ahn et al., 2021) (on the right) and two GPTS models (Ogg, 2020; Sahy et al., 2017) (on the top) are also shown. The black triangles indicate putative excursions Ahn et al. (2021) identified.

4 Discussion

4.1 Age correlation with geomagnetic polarity time scale

Here, we compare our high-precision groundmass-derived ages and the previously reported high-precision sanidine single-crystal-derived ages (Rochette et al., 1998) with the geomagnetic polarity ages of two GPTS models (Sahy et al., 2017; Ogg, 2020). The GPTS model of Ogg (2020) is the latest version of the GPTS. This GPTS model provides ages of geomagnetic reversal boundaries based on marine magnetic anomalies since the middle Mesozoic, which is constrained by astronomical tuning. The GPTS model of Sahy et al. (2017) was constructed by minimizing the discrepancy between the age-depth model based on U-Pb ages and the GPTS model of Ogg (2020). All $^{40}Ar/^{39}Ar$ ages here are recalibrated using the FCs standard with the age of 28.201 Ma (Kuiper et al., 2008) and the ^{40}K decay constant (Min et al., 2000) (Table S3). We can distinguish our two $^{40}Ar/^{39}Ar$ ages (samples A1-61 and A2-162 from the R4 magnetozone) at the 2σ level (29.82 ± 0.14 Ma and 30.21 ± 0.22 Ma, respectively). The age of sample A1-61 is correspond to Chron C11n.2n of GPTS2020, but this is not consistent with the polarity (Fig. 2b). In Sahy and other's GPTS model, the age of sample A1-61 is consistent with Chron C11r age at the 2σ level (Fig. 2b). The previous high precision sanidine single-crystal age of the sample LLC (29.9 ± 0.1 Ma) (recalibrated from Rochette et al., 1998) agrees with our age of sample A1-61 at almost the same elevation (~3200 m), indicating that our groundmass age has the similar accuracy and precision as the sanidine single-crystal age. Besides, the age of sample LLC agrees with Chron C11r of both GPTS models at the 2σ level (Fig. 2b) and the age of sample A2-162 agrees with Chron C11r of both GPTS models (Fig. 2b). Given these, we can interpret that all of the reversed polarity lava sequences at elevations between 2300 m and 3300 m (the R4 magnetozone) erupted in Chron C11r.

We can interpret that the Lima-Limo section erupted over Chrons C12r and C11r based on the eruption age models calculated from radiometric ages compiled from this study and previous studies (Fig. 2b, Table S4). This means that the Lima-Limo section erupted between 31.7 and 29.8 Ma (maximum estimation). The age model using our ages and the sanidine single-crystal ages of Rochette et al. (1998), which have high precision, agree with the age model constructed from all $^{40}Ar/^{39}Ar$ ages. This means that our ages and those of Rochette et al. (1998) contribute highly to the the age model constraints. The top of the age model constructed from all ages (3220 m) overlaps with Chron C11r of both GPTS models at the 95% confidence intervals, but it does not overlap with Chron C11n.1r of both GPTS models. This indicates that the lava flow of the magnetozone R4 erupted during Chron C11r. The N3–R4 magnetozone boundary of the age model constructed from all ages (2280 m) overlaps with the C12n–C11r boundary of the GPTS model of

Sahy et al. (2017) at the 95% confidence interval level, while it does not overlap with the boundary of Ogg (2020). The R1–N1 magnetozone boundary (1810 m) does not overlap with C12r–C12n boundary at the 95% confidence intervals of both GPTS models. This discrepancy suggests that the eruption rate around the R1–N1 magnetozone boundary may have been low. This possibility is consistent with the results that there are lava flows with intermediate paleomagnetic directions between the magnetozones N3 and R4, but not between R1 and N1 (Ahn et al., 2021). The bottom of the age model constructed from all ages (1330 m) overlaps with Chron C12r of the GPTS model of Ogg (2020) at the 95% confidence intervals, while it does not overlap with C12r of the GPTS model of Sahy et al. (2017). This indicates that the lava flow of the magnetozone R1 erupted during Chron C12r. In summary, the lava flows of the magnetozone R1 belong to Chron C12r, the those of the magnetozones N1 to N3 belong to Chron C12n, and the those of the magnetozone R4 belong to Chron C11r. We have uniquely correlated the Lima-Limo section to the GPTS for the first time.

We cannot correlate the short-lived reversed-polarity lava flows, R2 and R3 magnetozones (‘Lima-Limo reversals’), to Chron C12n of both GPTS models because Chron C12n does not include cryptochrons or excursions on the current GPTS. We now consider two possibilities for these reversed-polarity magnetozones. The first possibility is that we identified four new geomagnetic reversals within Chron C12n that have not been previously detected from marine magnetic anomalies (Cande and Kent, 1992). In this case, there would be a short reversal polarity in Chron C12n that has not yet been registered in GPTS. In the Waja section that erupted in Chron C12n (Eid et al., 2021), intermediate paleomagnetic directions were reported from six lava flows. The six lava flows are located in the lower part of the Waja section, which suggests that the paleomagnetic direction in early C12n is unstable. This finding is consistent with the R2 and R3 magnetozones found in the Lima-Limo section. A relative paleomagnetic intensity low in the early C12n observed in Oligocene marine sediments (Yamazaki et al., 2013; Yamamoto et al., 2014) may reflect the Lima-Limo reversals, suggesting that this is a global event. In addition, the absolute paleointensity decrease was observed in the N1 magnetozone (Yoshimura et al., 2020). Thus, we interpreted that geomagnetic reversals occurred in early Chron C12n. The second possibility is that the lavas in the R2 and R3 magnetozones are intrusive rocks formed at different times than the upper and lower lava. When we conducted the field survey at the Lima-Limo section, however, we did not find any dyke or sill in the lava outcrops (Fig. S1). Therefore, we consider that the geomagnetic reversals of the R2 and R3 magnetozones reflect the geomagnetic field behavior in early Chron C12n.

4.2 Estimation of emplacement rate

We calculate the eruption rate for each chron to calculate the eruption rate using the volume of 150000 km^3 of tholeiitic basalt in the LT basalt zone estimated in a previous study (Beccaluva et al., 2009). This is about 20% of the total volume of the Ethiopia–Yemen Traps (Rooney, 2017) of 720000 km^3. In this case, the volume of magnetozone R4 is calculated to be 71484 km^3, N1 to N3 is 31524 km^3, and R1 is 46992 km^3. We assume that the maximum eruption durations are as follows: 0.621 Myr (Ogg, 2020) or 0.50 Myr (Sahy et al., 2017) for the R4 magnetozone (Chron C11r), 0.386 Myr (Ogg, 2020) or 0.82 Myr (Sahy et al., 2017) for the N1 to N3 magnetozones, and 2.237 Myr (Ogg, 2020) or 1.86 Myr (Sahy et al., 2017) for the R1 magnetozone. Based on these maximum durations, the eruption rates are calculated as 0.02 to 0.03 km^3/yr for the R1 magnetozone, 0.04 to 0.08 km^3/yr for the N1 to N3 zone, and 0.12 to 0.14 km^3/yr for the R4 magnetozone, respectively (Table S5). Note that it is unclear when the eruption of the R1 magnetozone began. According to our age model, the lavas of the magnetozone R1 are likely to start eruption in late Chron C12r (Fig. 2b). However, this inference is not precise enough to calculate the eruption rate of the R1 magnetozone. Therefore, it is also necessary to estimate the eruption rate in the paleomagnetic directional groups (DGs).

To determine the net duration of the eruptive period of the Lima-Limo section, we use the results of the analysis of paleomagnetic secular variations recorded in the section (Ahn et al., 2021). Ahn et al. (2021) used the method proposed by Mankinen et al. (1985) and the statistical test of McFadden and Lowes (1981). They then grouped the statically same directions and assigned 11 DGs. However, site-averaged directions with α95 exceeding ten were used for two DGs, so only nine DGs are used in this study. We assume that the rate of geomagnetic secular variations in the last 3000 years (~2 °/100 years, Chenet et al., 2008) and that in the Lima-Limo section are the same. Because lava flows record the ambient geomagnetic direction during cooling, we can infer whether the paleomagnetic directions of successive lava flows were separated by long time intervals using paleomagnetic secular variations. Lava flows separated by long time intervals usually have significantly different mean paleomagnetic directions, but when erupted successively within a short time interval, such as 100 years, they are statistically indistinguishable. If the mean directions of adjacent lava flows are statistically indistinguishable at the 95% confidence level, the lava flows are considered to have been rapidly emplaced and failed to record paleomagnetic secular variations. Their paleomagnetic directions are merged into a single DG (Chenet et al., 2008). We assumed the upper and lower limits of lava eruption time for individual DGs as 100 years and ten years, respectively, and the interval of lava flows that have distinct paleomagnetic directions as at least 500 years (Chenet et al., 2008). In this case, for the entire Lima-Limo section, the eruption period of the R1 magnetozone corresponding to Chron C12r is 2 × 10 (100) + 20 × 500 = 10020 (10200) years at least (at most). Through the same calculation manner, that of the N1 to N3 magnetozones is 7010–7100 years, and that of the R4 magnetozone is 11550 –12000 years. The eruption rates can be estimated to be 4.61–4.69 km^3/yr for the magnetozone R1, 4.44–4.50 km^3/yr for the magnetozones N1 to N3, and 5.96–6.19 km^3/yr for the magnetozone R4, respectively (Table S5). Note that the relatively high eruption rate of the magnetozone R4 would be slightly overestimated because sampling densities were sparse due to poor exposures at ~2640–2740 and ~2900–3040 m and entrance restrictions at 3120–3260 m (Ahn et al., 2021). Nevertheless, these rates are lower than the previous estimation for HT2 lavas (4–13 km^3/yr: Eid et al., 2021).

4.3 Edge-driven convection to induce partial melting of ambient (non-plume) asthenosphere

The HT2 lavas reported in a previous study (Pik et al., 1998) are thought to represent the mantle plume axis (Natali et al., 2016). The HT2 lava flows were the first zone to erupt in three titanium zones and had the highest emplacement rate of 4–13 km^3/yr in the Oligocene Ethiopia–Yemen Traps, which is thought to be the Afar plume head expression (Eid et al., 2021). The HT1 zone shows a circular pattern around the HT2 zone (Fig. 1a) (Beccaluva et al., 2009; Natali et al., 2016). The mantle potential temperatures of each zone are consistent with the expected plume head temperature distribution (Beccaluva et al., 2009; Natali et al., 2016). However, we found that the LT lavas erupted earlier than the HT2 lavas and had a lower eruption rate than the HT2 lavas (Fig. 3a, b). In other words, the LT zone would have been the first eruption in the Oligocene Ethiopia–Yemen Traps, even though it was not on the plume head axis. Additionally, the emplacement rate of the LT lavas was lower than that of the HT2 lavas. Given that the Lima-Limo and Belessa section, the eruption period of the LT lavas (Chron C12r to C11n.1n) appears to have been significantly longer than that of the HT2 lavas (Chron C12n) (Fig. 3a). These results are contrary to the geodynamic model which predicts that the first stage of the plume eruption is the most vigorous. If the plume head collides with a lithosphere with a simple structure, then eruptions caused by the plume head should be spatially simultaneous. However, this is not the case in the Afar region.

We propose that this discrepancy in eruption timing was caused by the interaction of the Afar plume with the lithospheric basement topography. The first scenario is that a part of the plume reached the near-surface earlier than the plume head axis. When there is a gradient of the lithospheric thickness (i.e., lithospheric step), the plume would flow and rise along the lithospheric step from a thicker part to a thinner part (e.g., Thompson and Gibson, 1991; Ebinger and Sleep, 1998; Gorczyk et al., 2018). In the Afar plume case, we assume that the lithosphere under the LT zone was thin, and the lithosphere under the HT2 zone was thick. It is difficult to verify the lithospheric step under the Afar basement that once may have existed because the lithospheric thickness at present is considered to have been increased by the Afar plume accretion. Nnonetheless, this is possible because the lithospheric thickness can have large spatial variations (e.g., Globig et al., 2016). After the Afar plume collided with the lithosphere, a part of the plume flowed into the thinner lithosphere under the LT zone (Fig. 3c–e). This induced decompression melting of the asthenosphere to produce the HT magma. However, little plume signals have been found in the LT lava (Marty et al., 1996; Pik et al., 2006). Thus, the flood basalts in the LT zone may not be explained by the decompression melting of the plume head. The second scenario is that edge-driven convection occurred when the Afar plume rose (Fig. 3f–h). Edge-driven convection is an asthenospheric small-scale convective instabiliy caused by lithospheric steps (e.g., King and Anderson, 1998). Numerical simulations suggested that edge-driven convection presumably occurred at a lithospheric step near the plume before the collision of the plume at the lithosphere–asthenosphere boundary (Duvernay et al., 2022); when a lithospheric step between the LT and HT2 zones was present, edge-driven convection would have induced partial melting of the ambient (non-plume) asthenosphere to produce LT magma (Fig. 3g). Also, this scenario is consistent with little plume signal found in the lavas of the LT zone. Furthermore, we can explain the lower emplacement rate of the LT lavas than that of the HT2 lavas because the emplacement was not caused by the impact of the main body of the plume head (Fig. 3b). This scenario can successfully explain the absence of LT lavas in the eastern part of the East African Main Rift and the Yemen area (Pik et al., 1998) and the asymmetric shape of the Afar plume (Beccaluva et al., 2009). The interaction between the mantle plumes and the continental lithospheric geometry in the scenario may occur universally when a plume rises.

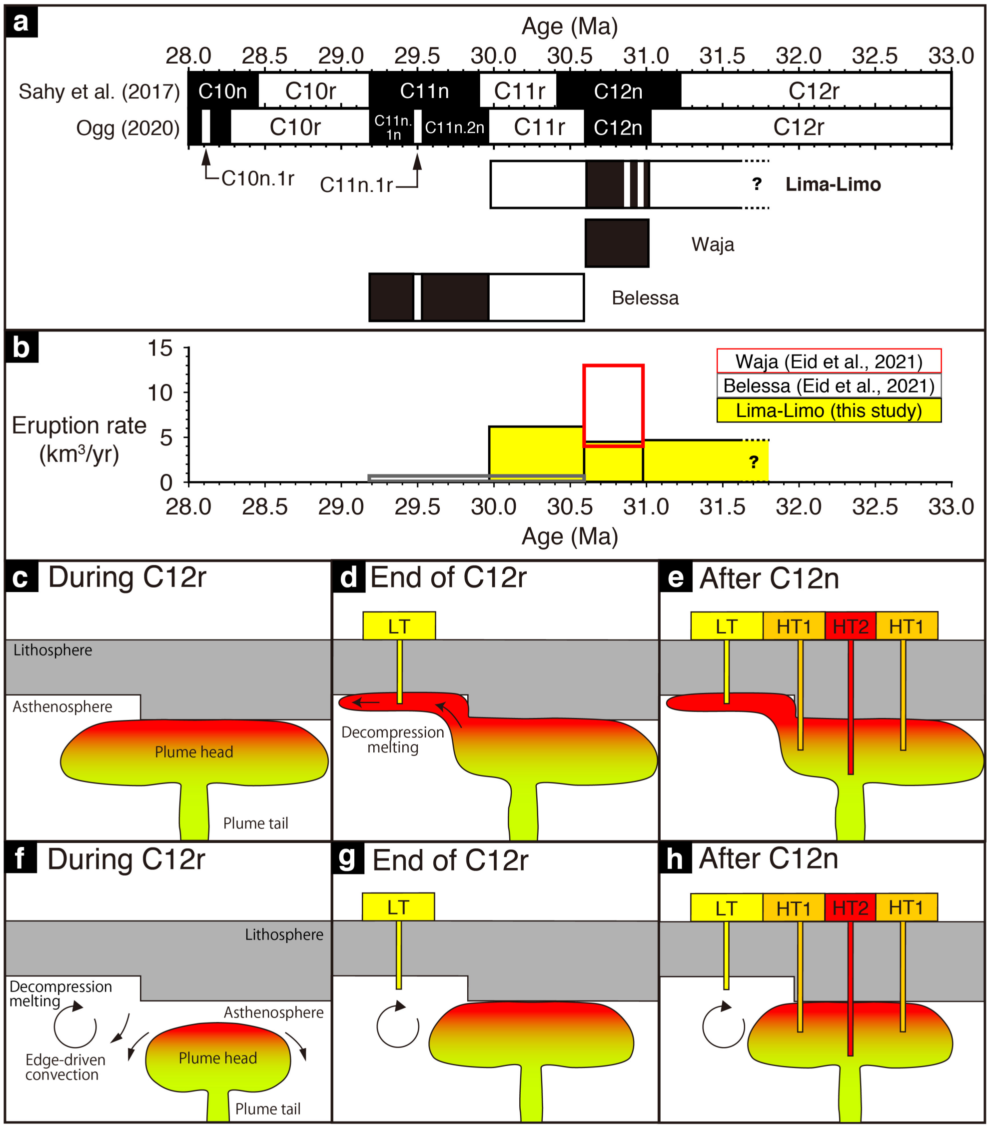

Figure 3. (a) Emplacement order of the Lima-Limo, Waja, and Belessa sections with the geomagnetic polarity time scales (Sahy et al., 2017; Ogg, 2020). (b) Eruption rates of each section. (c–e) Schematic illustration of the Afar plume rise and emplacement of the Traps by the decompression melting. (c) The Afar plume collides with the lithosphere. (d) A part of the Afar plume flows into the thinner lithosphere. The part of the plume rises along the lithosphere, which causes decompression melting. (e) Subsequently, the hot plume head center melts, which forms the HT1 and HT2 basalts. We assume that HT1 and HT2 erupted simultaneously. (f–h) Schematic illustration of the Afar plume rise and emplacement of the Traps by edge-driven convection. (f) When the Afar plume approaches the surface, edge-driven convection occurs near a lithosphere step. Edge-driven convection causes decompression melting of ambient (non-plume) asthenosphere. (g) The decompression melting produces the first magma of the Oligocene Afar

plume, the LT lavas. (h) Subsequently, the hot plume head center melts, which forms the HT1 and HT2 basalts.

5 Conclusion

We conclude that the Oligocene Ethiopia–Yemen Traps in the Lima-Limo section erupted over Chrons C12r–C12n–C11r considering new high-precision $^{40}Ar/^{39}Ar$ ages and previously reported $^{40}Ar/^{39}Ar$ ages. The four geomagnetic reversals observed in the Chron C12n lava flow may be short geomagnetic reversals within Chron C12n. The LT lavas in the Lima-Limo section emplaced before the main pulse of Afar magmatism, the eruption of the HT2 lavas. The eruption rate of the Lima-Limo section was lower than that of HT2 lavas. Since little plume component is detected for the LT lavas, we suggest that the partial melting of ambient (non-plume) asthenosphere to produce the LT magmas was induced by edge-driven convection in the asthenosphere, which occurred before the plume head reached the lithosphere.

Acknowledgements

We thank Yusuke Suganuma, Kenichiro Tani, Hironao Matsumoto, Masakazu Fujii, Naoto Fukuyo, and Takashi Sano for their helpful suggestions. We thank Ryo Okumura, Hisao Yoshinaga, and Yuto Iinuma for irradiation of dated samples at KUR, Institute for Integrated Radiation and Nuclear Science, Kyoto University and Fumihiko Ikegami for making geological maps from the GEBCO2014 grid using QGIS. Y.Yoshimura was supported by Grant-in-Aid (Early-Career Scientists) (No. 22K14124), and O.I. was supported by Grant-in-Aid (C) (No. 17K05686) provided by JSPS. H.-S.A. was supported by grants from KIGAM (GP2022-006 and GP2021-006).

Data Availability

All new data used in the figures are included in supporting information files. The $^{40}Ar/^{39}Ar$ data will be available at the Kyushu University Institutional Repository (QIR) before the publication.

References

Ahn, H. S., Kidane, T., Otofuji, Y., Yamamoto, Y., Ishikawa, N., & Yoshimura, Y. (2021). High-resolution palaeomagnetic results of Ethiopian trap series from Lima Limo section: implications for the Oligocene geomagnetic field behaviour and timing of volcanism. Geophysical Journal International, 225(1), 311-328.

Beccaluva, L., Bianchini, G., Natali, C., & Siena, F. (2009). Continental flood basalts and mantle plumes: a case study of the Northern Ethiopian Plateau. Journal of Petrology, 50(7), 1377-1403.

Blaauw, M., & Christen, J. A. (2011). Flexible paleoclimate age-depth models using an autoregressive gamma process. Bayesian analysis, 6(3), 457-474.

Bosworth, W., Huchon, P., & McClay, K. (2005). The red sea and gulf of aden basins. Journal of African Earth Sciences, 43(1-3), 334-378.

Boyce, A., Bastow, I. D., Cottaar, S., Kounoudis, R., Guilloud De Courbeville, J., Caunt, E., & Desai, S. (2021). AFRP20: New P-wavespeed model for the African mantle reveals two whole-mantle plumes below East Africa and neoproterozoic modification of the Tanzania Craton. Geochemistry, Geophysics, Geosystems, 22(3), e2020GC009302.

Cande, S. C., & Kent, D. V. (1992). A new geomagnetic polarity time scale for the Late Cretaceous and Cenozoic. Journal of Geophysical Research, 97(B10), 13917-13951.

Cande, S. C., & Kent, D. V. (1995). Revised calibration of the geomagnetic polarity timescale for the Late Cretaceous and Cenozoic. Journal of Geophysical Research, 100(B4), 6093-6095.

Chenet, A. L., Fluteau, F., Courtillot, V., Gérard, M., & Subbarao, K. V. (2008). Determination of rapid Deccan eruptions across the Cretaceous-Tertiary boundary using paleomagnetic secular variation: Results from a 1200-m-thick section in the Mahabaleshwar escarpment. Journal of Geophysical Research: Solid Earth, 113(B4).

Coulié, E., Quidelleur, X., Gillot, P. Y., Courtillot, V., Lefèvre, J. C., & Chiesa, S. (2003). Comparative K–Ar and Ar/Ar dating of Ethiopian and Yemenite Oligocene volcanism: implications for timing and duration of the Ethiopian traps. Earth and Planetary Science Letters, 206(3-4), 477-492.

Duvernay, T., Davies, D. R., Mathews, C., Gibson, A. H., & Kramer, S. C. (2022). Continental Magmatism: The Surface Manifestation of Dynamic Interactions Between Cratonic Lithosphere, Mantle Plumes and Edge-Driven Convection.

Ebinger, C. J., & Sleep, N. H. (1998). Cenozoic magmatism throughout east Africa resulting from impact of a single plume. Nature, 395(6704), 788-791.

Eid, B., Lhuillier, F., Gilder, S. A., Pfänder, J. A., Gebru, E. F., & Aßbichler, D. (2021). Exceptionally high emplacement rate of the afar mantle plume head. Geophysical Research Letters, 48(23), e2021GL094755.

French, S. W., & Romanowicz, B. (2015). Broad plumes rooted at the base of the Earth's mantle beneath major hotspots. Nature, 525(7567), 95-99.

Globig, J., Fernàndez, M., Torne, M., Vergés, J., Robert, A., & Faccenna, C. (2016). New insights into the crust and lithospheric mantle structure of Africa from elevation, geoid, and thermal analysis. Journal of Geophysical Research: Solid Earth, 121(7), 5389-5424.

Gorczyk, W., Mole, D. R., & Barnes, S. J. (2018). Plume-lithosphere interaction at craton margins throughout Earth history. Tectonophysics, 746, 678-694.

Hofmann, C., Courtillot, V., Feraud, G., Rochette, P., Yirgu, G., Ketefo, E., & Pik, R. (1997). Timing of the Ethiopian flood basalt event and implications for plume birth and global change. Nature, 389(6653), 838-841.

Huestis, S. P., & Acton, G. D. (1997). On the construction of geomagnetic timescales from non-prejudicial treatment of magnetic anomaly data from multiple ridges. Geophysical Journal International, 129(1), 176-182.

Ishizuka, O., Hickey-Vargas, R., Arculus, R. J., Yogodzinski, G. M., Savov, I. P., Kusano, Y. et al. (2018). Age of Izu–Bonin–Mariana arc basement. Earth and Planetary Science Letters, 481, 80-90.

Kieffer, B., Arndt, N., Lapierre, H., Bastien, F., Bosch, D., Pecher, A. et al. (2004). Flood and shield basalts from Ethiopia: magmas from the African superswell. Journal of Petrology, 45(4), 793-834.

King, S. D., & Anderson, D. L. (1998). Edge-driven convection. Earth and Planetary Science Letters, 160(3-4), 289-296.

Kuiper, K. F., Deino, A., Hilgen, F. J., Krijgsman, W., Renne, P. R., & Wijbrans, A. J. (2008). Synchronizing rock clocks of Earth history. Science, 320(5875), 500-504.

Lhuillier, F., & Gilder, S. A. (2019). Palaeomagnetism and geochronology of Oligocene and Miocene volcanic sections from Ethiopia: geomagnetic variability in the Afro-Arabian region over the past 30 Ma. Geophysical Journal International, 216(2), 1466-1481.

Mankinen, E. A., Prevot, M., Grommé, C. S., & Coe, R. S. (1985). The Steens Mountain (Oregon) geomagnetic polarity transition: 1. Directional history, duration of episodes, and rock magnetism. Journal of Geophysical Research: Solid Earth, 90(B12), 10393-10416.

Marty, B., Pik, R., & Gezahegn, Y. (1996). Helium isotopic variations in Ethiopian plume lavas: nature of magmatic sources and limit on lower mantle contribution. Earth and Planetary Science Letters, 144(1-2), 223-237.

McFadden, P. L., & Lowes, F. J. (1981). The discrimination of mean directions drawn from Fisher distributions. Geophysical Journal International, 67(1), 19-33.

Min, K., Mundil, R., Renne, P. R., & Ludwig, K. R. (2000). A test for systematic errors in $^{40}Ar/^{39}Ar$ geochronology through comparison with U/Pb analysis of a 1.1-Ga rhyolite. Geochimica et Cosmochimica Acta, 64(1), 73-98.

Mohr, P. (1983). Ethiopian flood basalt province. Nature, 303(5918), 577-584.

Mohr, P., & Zanettin, B. (1988). The Ethiopian flood basalt province. Continental flood basalts, 63-110.

Natali, C., Beccaluva, L., Bianchini, G., Ellam, R. M., Savo, A., Siena, F., & Stuart, F. M. (2016). High-MgO lavas associated to CFB as indicators of plume-related thermochemical effects: The case of ultra-titaniferous picrite–basalt from the Northern Ethiopian–Yemeni Plateau. Gondwana Research, 34, 29-48.

Ogg, J. G. (2020). Geomagnetic polarity time scale. Geologic time scale 2020, pp. 159–192, eds Gradstein, F.M., Elsevier.

Ogg, J. G., Ogg, G. M., & Gradstein, F. M. (2016). A concise geologic time scale: 2016.

Pik, R., Deniel, C., Coulon, C., Yirgu, G., Hofmann, C., & Ayalew, D. (1998). The northwestern Ethiopian Plateau flood basalts: classification and spatial distribution of magma types. Journal of Volcanology and Geothermal Research, 81(1-2), 91-111.

Pik, R., Marty, B., & Hilton, D. R. (2006). How many mantle plumes in Africa? The geochemical point of view. Chemical Geology, 226(3-4), 100-114.

Prave, A. R., Bates, C. R., Donaldson, C. H., Toland, H., Condon, D. J., Mark, D., & Raub, T. D. (2016). Geology and geochronology of the Tana Basin, Ethiopia: LIP volcanism, super eruptions and Eocene–Oligocene environmental change. Earth and Planetary Science Letters, 443, 1-8.

Rooney, T. O. (2017). The Cenozoic magmatism of East-Africa: Part I—Flood basalts and pulsed magmatism. Lithos, 286, 264-301.

Rochette, P., Tamrat, E., Féraud, G., Pik, R., Courtillot, V., Ketefo, E., Coulon, C., Hofmann, C., Vandamme, D., & Yirgu, G. (1998). Magnetostratigraphy and timing of the Oligocene Ethiopian traps. Earth and Planetary Science Letters, 164(3-4), 497-510.

Sahy, D., Condon, D. J., Hilgen, F. J., & Kuiper, K. F. (2017). Reducing disparity in radio-isotopic and astrochronology-based time scales of the Late Eocene and Oligocene. Paleoceanography, 32(10), 1018-1035.

Schaen, A. J., Jicha, B. R., Hodges, K. V., Vermeesch, P., Stelten, M. E., Mercer, C. M. et al. (2021). Interpreting and reporting 40Ar/39Ar geochronologic data. GSA Bulletin, 133(3-4), 461-487.

Sprain, C. J., Renne, P. R., Vanderkluysen, L., Pande, K., Self, S., & Mittal, T. (2019). The eruptive tempo of Deccan volcanism in relation to the Cretaceous-Paleogene boundary. Science, 363(6429), 866-870.

Thompson, R. N., & Gibson, S. A. (1991). Subcontinental mantle plumes, hotspots and pre-existing thinspots. Journal of the Geological Society, 148(6), 973-977.

Yamamoto, Y., Yamazaki, T., Acton, G. D., Richter, C., Guidry, E. P., & Ohneiser, C. (2014). Palaeomagnetic study of IODP Sites U1331 and U1332 in the equatorial Pacific—extending relative geomagnetic palaeointensity observations through the Oligocene and into the Eocene. Geophysical Journal International, 196(2), 694-711.

Yamazaki, T., Yamamoto, Y., Acton, G., Guidry, E. P., & Richter, C. (2013). Rock-magnetic artifacts on long-term relative paleointensity variations in sediments. Geochemistry, Geophysics, Geosystems, 14(1), 29-43.

Yoshimura, Y., Yamazaki, T., Yamamoto, Y., Ahn, H. S., Kidane, T., & Otofuji, Y. (2020). Geomagnetic paleointensity around 30 Ma estimated from Afro-Arabian Large Igneous Province. Geochemistry, Geophysics, Geosystems, 21(12), e2020GC009341.

References from the supporting information

Uchiumi, S., & Shibata, K. (1980). Errors in K-Ar age determination. Bulletin of Geological Survey of Japan, 31(6), 267-273.

Fleck, R. J., Sutter, J. F., & Elliot, D. H. (1977). Interpretation of discordant $^{40}Ar/^{39}Ar$ age-spectra of Mesozoic tholeiites from Antarctica. Geochimica et Cosmochimica Acta, 41(1), 15-32.

York, D., Evensen, N. M., Martınez, M. L., & De Basabe Delgado, J. (2004). Unified equations for the slope, intercept, and standard errors of the best straight line. American Journal of Physics, 72(3), 367-375.